Available online at www.sciencedirect.com
SciVerse ScienceDirect
Acta Materialia 61 (2013) 4607–4618
Acta MATERIALIA
www.elsevier.com/locate/actamat

# Hydrogen-assisted failure in a twinning-induced plasticity steel studied under in situ hydrogen charging by electron channeling contrast imaging

Motomichi Koyama [a,b,*], Eiji Akiyama [b], Kaneaki Tsuzaki [b,c], Dierk Raabe [a]

[a] Max-Planck-Institut für Eisenforschung GmbH, Max-Planck-Straße 1, 40237 Düsseldorf, Germany
[b] National Institute for Materials Science, 1-2-1, Sengen, Ibaraki 305-0047, Japan
[c] Department of Mechanical Engineering, Kyushu University, 744 Motooka, Nishi-ku, Fukuoka 819-0395, Japan

Received 11 February 2013; received in revised form 4 April 2013; accepted 13 April 2013
Available online 9 May 2013

**Abstract**

We investigated the hydrogen embrittlement of a Fe–18Mn–1.2%C (wt.%) twinning-induced plasticity steel, focusing on the influence of deformation twins on hydrogen-assisted cracking. A tensile test under ongoing hydrogen charging was performed at low strain rate ($1.7 \times 10^{-6}$ s$^{-1}$) to observe hydrogen-assisted cracking and crack propagation. Hydrogen-stimulated cracks and deformation twins were observed by electron channeling contrast imaging. We made the surprising observation that hydrogen-assisted cracking was initiated both at grain boundaries and also at deformation twins. Also, crack propagation occurred along both types of interfaces. Deformation twins were shown to assist intergranular cracking and crack propagation. The stress concentration at the tip of the deformation twins is suggested to play an important role in the hydrogen embrittlement of the Fe–Mn–C twining-induced plasticity steel.


*Keywords:* Twinning-induced plasticity (TWIP) steel; Mechanical properties; Hydrogen embrittlement; Crack propagation; Electron channeling contrast imaging

## 1. Introduction

Understanding the hydrogen-assisted embrittlement of advanced structural materials is essential for enabling future hydrogen-based energy industries. A crucially important phenomenon in this context is the delayed fracture in high-strength structural materials. Factors affecting the hydrogen embrittlement have been reported to be the hydrogen content [1–3], residual stress (as well as applied stress) [3–5] and microstructure [5–8]. These factors can all lead to a critical condition for hydrogen embrittlement through specific mechanisms, e.g. hydrogen-induced decohesion [9–11], hydrogen-enhanced strain-induced vacancy formation [12] and hydrogen-enhanced localized plasticity [13–16].

In this work we study the mechanisms of hydrogen embrittlement in a new class of steels, namely Fe–Mn–C twinning-induced plasticity (TWIP) steels. These materials present a new group of advanced high-strength and formable austenitic steels with high potential for automotive forming applications [17,18]. Moreover, energy-related infrastructures and pipelines are envisaged as future applications of these steels [19]. Hydrogen embrittlement of TWIP steels was observed in the form of delayed fracture tests in cup-drawn specimens under air [18,20] and also in tensile tests with cathodically hydrogen-charged specimens [21–26]. Clarifying the mechanism of the respective hydrogen embrittlement of TWIP steels is an essential pending problem. The effects of hydrogen content [23,25,26] and residual stress (as well as of the applied stress) [20,23,25]

* Corresponding author at: Max-Planck-Institut für Eisenforschung GmbH, Max-Planck-Straße 1, 40237 Düsseldorf, Germany. Tel.: +49 211 6792 885; fax: +49 211 6792 333.
*E-mail address:* m.koyama@mpie.de (M. Koyama).

1359-6454/$36.00 
http://dx.doi.org/10.1016/j.actamat.2013.04.030

have already been examined thoroughly. However, the effect of the corresponding microstructures is still under debate due to the complexity of the phenomena and boundary conditions involved [27]. Microstructures affecting the hydrogen embrittlement of TWIP steels have been reported to be dislocation density [25], martensite content [28], and deformation twins [29]. Chun et al. have clarified the influences of the dislocation density [25] and of martensite [28]. In contrast, there have been only few reports on the effect of deformation twins, which are indispensable lattice defects governing the excellent formability of TWIP steels [17,18,27].

Deformation twinning is a characteristic phenomenon in face-centered cubic (fcc) materials with low stacking fault energy, and is reported to cause embrittlement even in non-hydrogen-charged steels [30,31]. In a previous study [29], the hydrogen-assisted cracking of a Fe–18Mn–1.2C TWIP steel (wt.%) was found to occur at deformation twin boundaries as well as at grain boundaries, although the precise mechanism was not revealed. Deformation twin boundary cracking was observed by electron channeling contrast imaging (ECCI) [29], which is an excellent method for detecting fine twins [32–34]. Since ECCI enables the visualization of deformation twins at a wide field of view compared to transmission electron microscopy, it is a suitable technique for investigating the correlation between deformation twinning and cracking on a mesoscopic scale. In particular, crack propagation associated with the occurrence of deformation twinning is expected to be clarified by the use of ECCI. For this purpose, we used a Fe–18Mn–1.2C steel that is known to show high strength in conjunction with exceptional elongation [35,36]. This specific TWIP steel does not contain any martensite even after it fractures at ambient temperature (294 K) due to its high carbon concentration [36]; however, hydrogen embrittlement occurs when it is exposed to tensile testing under hydrogen charging [29].

The aim of this study is to reveal how deformation twinning contributes to hydrogen-assisted cracking along both non-coherent grain boundaries and Σ3 coherent twin boundaries in a stable austenitic TWIP steel using ECCI. The main novelty of this approach lies in two fields: first, we conduct the tensile test directly under permanent electrochemical hydrogen charging; secondly, we use ECCI to map microstructure changes that result from hydrogen charging. This combined experimental approach enables tracking the microstructure at a wide field of view under minimum sample preparation requirements for imaging dislocation, twin and interface structures. This approach has advantages over the use of transmission electron microscopy owing to the wide field of view that ECCI offers.

## 2. Experimental

The Fe–18.0Mn–1.15C (wt.%) steel was prepared by induction melting. The ingot was forged and hot rolled at 1273 K. It was then solution treated at 1273 K for 3600 s under an argon atmosphere and subsequently water quenched to suppress carbide formation. The average grain size was 46 μm including the annealing twin boundaries. Tensile specimens with gauge dimensions of 4 mm wide × 0.5 mm thick × 10 mm long and grip sections on both ends were cut by spark erosion. The steel showed 80% uniform elongation and 1.2 GPa tensile strength due to deformation twinning [36]. In this study, we performed 10% tensile pre-straining before the test for hydrogen embrittlement to promote the effect of deformation twins on hydrogen embrittlement. Therefore, a considerable density of deformation twins was already introduced before the test. The details of the deformation microstructure of the present steel after 10% straining have been reported in a previous study [36].

The tensile test was conducted at ambient temperature around 294 K at an initial strain rate of $1.7 \times 10^{-6}\ s^{-1}$ along the rolling direction (RD) using an Instron machine. Strain determination was done by dividing the displacements by the initial gauge length. Hydrogen was continuously introduced into the specimens during the tensile tests by electrochemical charging in a 3% NaCl aqueous solution containing $3\ g\ l^{-1}$ of $NH_4SCN$ at a current density of $9\ A\ m^{-2}$ during the ongoing test. A platinum wire was used as counter-electrode. The solution was added continuously to cover the gauge part of the sample during the tensile tests. The specimen was covered by a plastic container containing the solution. The experimental set-up is shown schematically in Fig. 1. The hydrogen charging started along with the tensile test (in situ charging), and the hydrogen was introduced into the samples effectively via diffusion as well as through the motion of hydrogen-decorated dislocations [37,38]. The tensile tests under hydrogen charging was able to show the hydrogen embrittlement in TWIP steels successfully [21,23,29,39].

The hydrogen content introduced during the test was measured by the means of thermal desorption analysis (TDA) from room temperature to 550 K. TDA was

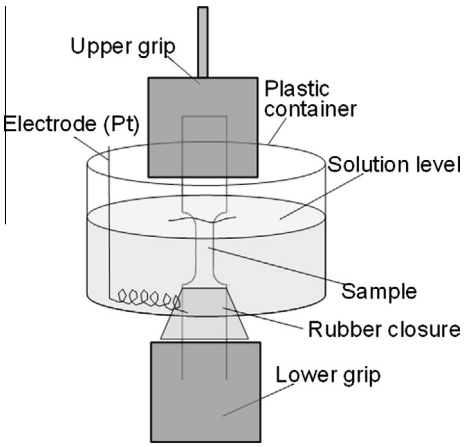


Fig. 1. A schematic of the set-up of in situ tensile test under ongoing hydrogen charging.

conducted immediately after the tensile test. The time that elapsed between the end of the tensile test and the start of the TDA analysis was below 20 min. The heating rate was 200 K $h^{-1}$. The diffusible hydrogen content was determined by measuring the cumulative desorbed hydrogen from room temperature up to 523 K. Diffusible hydrogen is defined as the amount of hydrogen that diffuses at room temperature. The diffusible hydrogen is reported to play a key role in hydrogen embrittlement [40].

Microstructure observations were performed by secondary electron imaging (SEI), electron back scattering diffraction (EBSD) and ECCI to observe hydrogen-assisted cracks and deformation twins. The specimens for the SEM observations were prepared by mechanical polishing with colloidal silica long enough to remove the layers affected by polishing with coarser particles. The SE and ECC imaging were operated at 15 kV. The EBSD analysis was operated at 20 kV with a beam step size of 300 nm or 1 μm. The microstructure observations were conducted 2 weeks after conducting the in situ hydrogen-charged tensile test. Since diffusible hydrogen was reported to be completely desorbed after exposure in air for 10 days [23], the diffusible hydrogen content of the present specimen was negligibly low when the microstructure was observed.

## 3. Results

### 3.1. Tensile test under ongoing hydrogen charging and observations of the main crack

Fig. 2 shows the engineering stress–strain curve obtained from the tensile test conducted in situ under hydrogen charging. The serrated flow on the stress–strain curve is caused by dynamic strain aging [41–46]. A main crack caused by the hydrogen uptake was observed at a plastic strain with about 19% elongation. The tensile test was stopped before the fracture. Fig. 3 shows a plot of

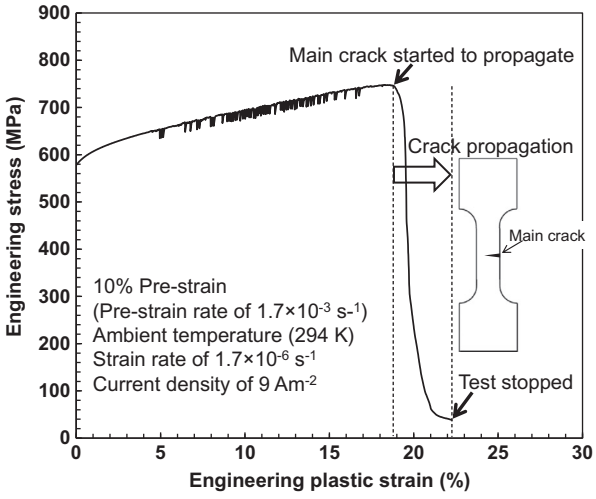


Fig. 2. Engineering stress–strain curve and its correspondence with cracking.

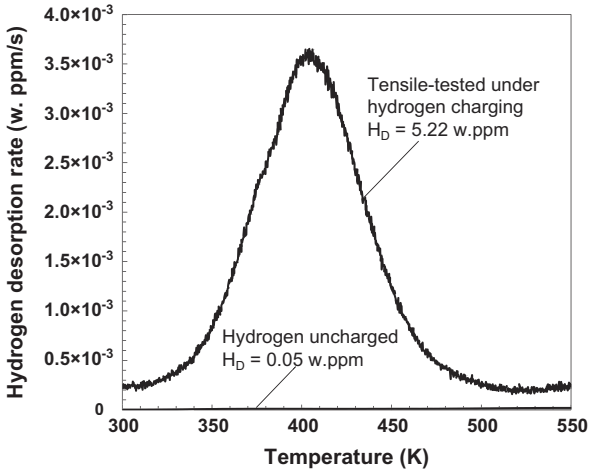


Fig. 3. Hydrogen desorption rate curve of the tensile-tested and the as-solution-treated specimens. $H_D$ indicates the diffusible hydrogen content.

the hydrogen desorption rate against temperature as obtained from the TDA. The peak corresponds to the desorption of diffusible hydrogen [23]. The diffusible hydrogen content was 5.22 wt. ppm after the tensile test under hydrogen charging.

Fig. 4 shows a SE image around the main crack. The main crack was initiated at the corners of the side edges of the specimen and propagated to the other side of the specimen. The direction of the macroscopic crack propagation was approximately perpendicular to the tensile axis. Additionally, a considerable number of subcracks were observed on the specimen surface as highlighted by the square. We followed the main crack path in our microstructure analysis in order to understand its propagation mechanism. The subcracks were also observed to investigate further crack initiation sites and to better understand the fine details of the crack propagation.

Fig. 5a shows an ECCI map of the region highlighted by the square in Fig. 4. The plate-like products appearing in white contrast are deformation twins [32], and the completely black contrast corresponds to the cracks. Deformation twins of fcc materials are generally accepted to have a

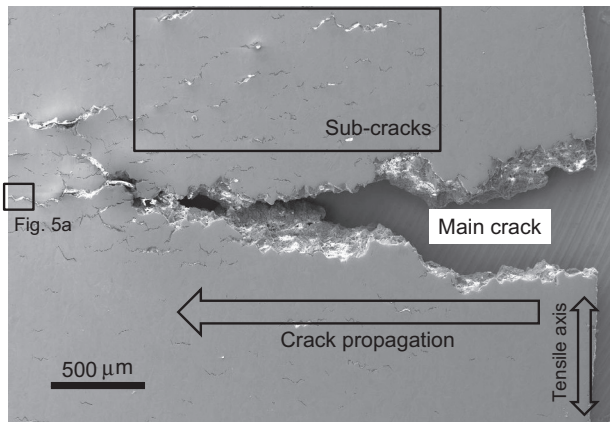


Fig. 4. Secondary electron image showing the main and subcracks.

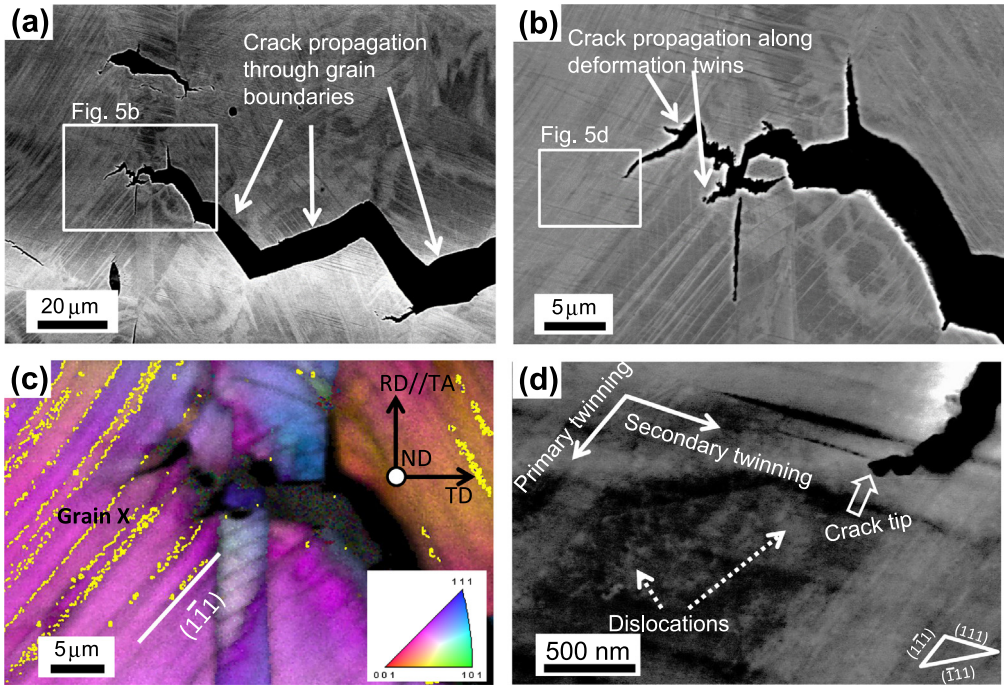


Fig. 5. (a) ECC image corresponding to the part highlighted by the square in Fig. 4. (b) Enlarged ECC image of (a). (c) RD-IPF map corresponding to (b). TA: Tensile axis. The yellow lines in (c) indicate Σ3 twin boundaries. (d) Orientation-optimized ECC image of the part highlighted in (b). (For interpretation of the references to color in this figure legend, the reader is referred to the web version of this article.)

plate-like shape, since they are formed by a displacive transformation on an {1 1 1} slip plane [27,47,48]. The crack propagation path is along the grain boundaries as indicated by the arrows. In addition, transgranular cracking is also observed around the tip of the main crack. Fig. 5b shows the magnified image of the region highlighted by the square in Fig. 5a. The ECCI analysis demonstrates that the crack propagates along the deformation twin boundaries as well as along the non-coincident grain boundaries and is also shown to intersect the deformation twin.

Fig. 5c shows the RD-inverse pole figure (IPF) map pertaining to Fig. 5b. The yellow lines indicate the Σ3 first-order twin boundaries. According to the result of the EBSD analysis, the normal direction (ND) and the RD (// tensile axis) of the parent crystal in grain X are [24 $\bar{1}$ 15] and [$\bar{5}$ $\bar{1}$ 5 7], respectively. The Schmid factors for preferential twinning shears on each twinning plane are summarized in Table 1. The deformation twins of grain X shown in Fig. 5c were determined to be primary twins from the viewpoint of the respective Schmid factor. Fig. 5d shows an orientation-optimized ECCI analysis conducted around the crack tip as highlighted by the square in Fig. 5b. When the orientation of the parent crystal is rotated to realize the optimized contrast under Bragg conditions, the parent crystal appears dark because of the low backscattering yield, while twins and dislocations are imaged in bright contrast due to their out-of-Bragg orientation [32]. The ECC image shows the primary and secondary twins clearly, and the dislocation substructure is observed in the dark region as indicated by the dotted arrows.

Table 1
Preferential twinning systems and their Schmid factors in grain X (Fig. 5c) with ND, RD orientations of [24 −1 15] and [−5 −15 7], respectively.

| Twinning plane | Preferential twinning direction | Schmid factor |
|---|---|---|
| (1 −1 1) | [−2 −1 1] | 0.429 |
| (−1 1 1) | [1 −1 2] | 0.057 |
| (1 1 −1) | [2 −1 1] | 0.255 |
| (1 1 1) | [−1 −1 2] | 0.348 |

### 3.2. Observations of subcracks associated with grain boundary and twin boundary cracking

Fig. 6 shows ECC images that exhibit intergranular cracking. In Fig. 6a, the intergranular cracking was initiated at grain boundary triple junctions. Fig. 6b reveals that cracking was initiated from the grain boundary where the deformation twins impinged. The intergranular cracking was observed to propagate not only perpendicular but also parallel to the tensile axis. Fig. 7 shows that the crack along the grain boundaries between grains A and B and between grains C and D propagated parallel to the tensile axis rather than perpendicularly to the tensile axis. From the viewpoint of the mode 1 fracture caused by uniaxial loading, the tensile stress is effectively applied on the grain boundary when the normal of the grain boundary is oriented towards the tensile axis. Thus, the intergranular

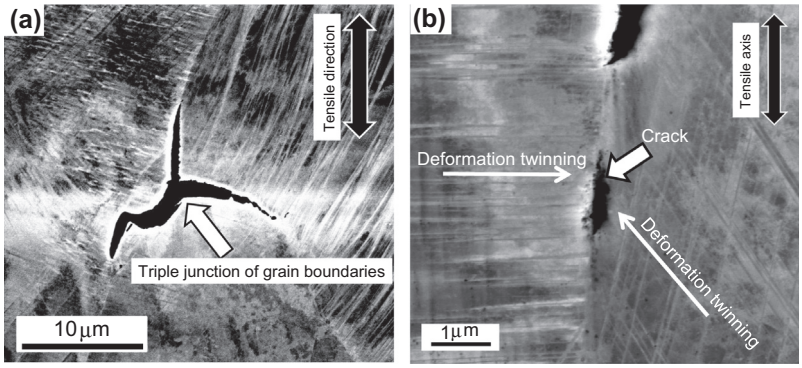


Fig. 6. Crack initiation from (a) a triple junction of the grain boundaries and (b) a grain boundary intercepting deformation twinning. These are the dominant crack initiation sites.

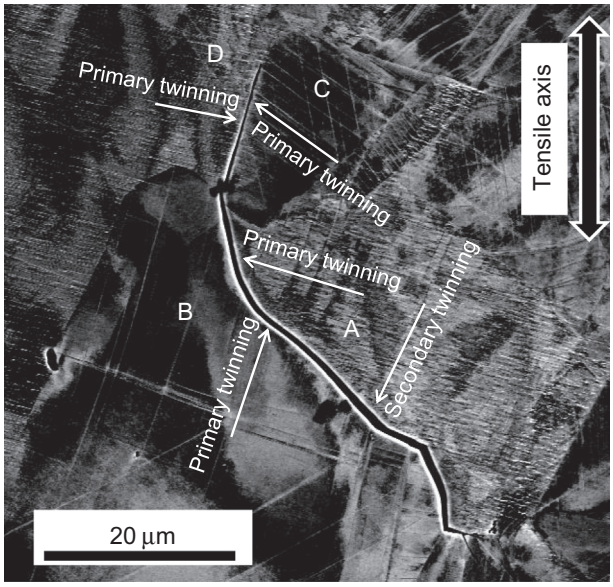


Fig. 7. ECC image showing intergranular cracking. Since this crack propagates only along the grain boundary, grain boundaries can be a crack initiation site. The arrows indicate the preferential twinning direction.

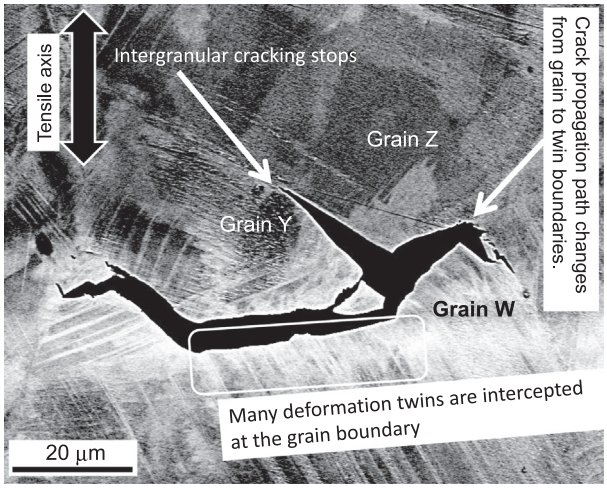


Fig. 8. ECC image showing crack propagation along a grain boundary. Interception of deformation twinning at the grain boundaries is often seen when cracks propagate along a grain boundary.

crack propagation proceeding nearly parallel to the tensile axis indicates the presence of an additional factor determining the cracking behavior. This point will be discussed in the next section.

Fig. 8 shows the crack propagation through some grains with various morphologies of the associated deformation twins. A number of these deformation twins were observed to impinge on the grain boundaries around the crack. One should note that only a small number of deformation twins were formed in grains Y and Z, and the deformation twins around the crack tip are nearly parallel to the grain boundary between grains Y and Z. In contrast, the deformation twins in grain W impinge on the grain boundary between grains W and Z. The cracking stops on the grain boundary between grains Y and Z. On the other hand, the propagation path associated with the grain boundary between grains W and Z changed from the non-coherent grain boundary onto the deformation twin boundaries in grain W.

Fig. 9a shows transgranular cracking through a set of grains. This transgranular defect propagated along primary and secondary deformation twins. As a result, the crack exhibits a zigzag-like morphology when following the deformation twin boundaries. According to the ECCI map that is shown exemplarily in Fig. 9, all of these brittle cracks proceed along a grain boundary or along deformation twin boundaries. This observation represents a general trend in the present study, namely, all of the transgranular subcracks were aligned parallel to the deformation twins. As shown in Fig. 9b, even the Σ3 coherent annealing twin boundaries suffered from hydrogen-assisted cracking. Fig. 10 shows a crack initiation event associated with deformation twins. The crack clearly exists within the grain and is caused by the interactions between blocked and obstacle deformation twins.

Fig. 11 shows the RD-IPF and ND-IPF maps taken in the subcracked part highlighted by the square in Fig. 4. The interfaces marked by black in the IPF maps indicate

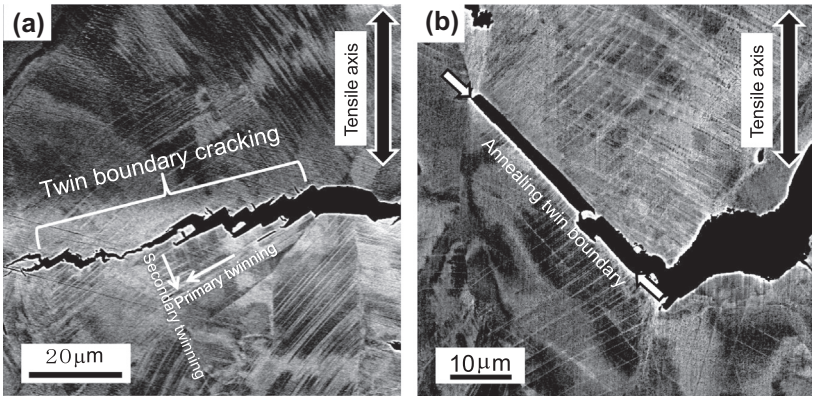


Fig. 9. ECC image showing crack propagation along (a) deformation twin boundaries and (b) an annealing twin boundary.

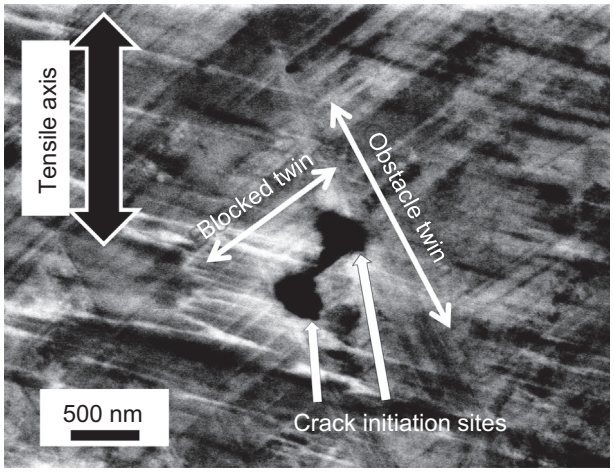


Fig. 10. ECC image showing transgranular crack initiation associated with deformation twins.

high-angle grain boundaries. Transgranular cracking highlighted by the solid white lines was observed dominantly in near-⟨1 1 1⟩ and ⟨1 1 0⟩-aligned tensile oriented grains. Intergranular cracking was almost never observed in cases where the tensile orientations of both grains involved were close to the ⟨1 0 0⟩ crystallographic axis, although the grain boundaries were typically high-angle grain boundaries, as highlighted by the broken white lines in Fig. 11a and b.

The ratio of the total crack propagation length along non-coherent grain boundaries relative to that along the twin boundaries was measured to be 3:1 (the percentage of twin boundary cracking was 25 ± 12%). The crack propagation length was determined by measuring the length of the subcracks as revealed in Fig. 4.

## 4. Discussion

### 4.1. Degradation of tensile properties

The Fe–18Mn–1.2C steel, when not exposed to hydrogen charging, is characterized by 80% uniform elongation and ductile fracture behavior at ambient temperature [29,35,36]. Therefore, we conclude that the drastic degradation in tensile elongation shown in Fig. 2 was caused by hydrogen uptake. The drop in maximum elongation is observed even more clearly when conducting the tensile test under ongoing hydrogen charging than in a tensile test carried out after hydrogen-precharging. For instance, Ronevich et al. reported [24] that the macroscopic tensile

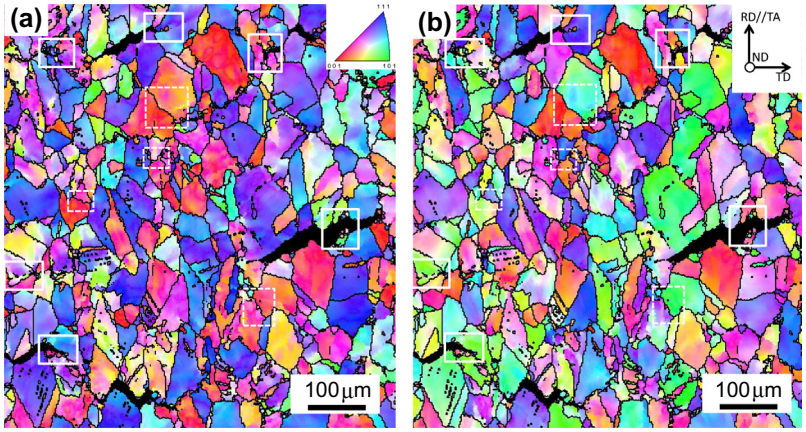


Fig. 11. (a) RD-IPF and (b) ND-IPF maps of the fractured specimen corresponding to the part of the subcracked region highlighted by the square in Fig. 4. The black grain boundaries indicate the high-angle grain boundaries ($15° < \theta < 180°$).

Table 2
Diffusible hydrogen contents of Fe–Mn–C ternary TWIP steels that showed significant degradation of tensile properties from previous results.

| Steel (wt.%) | Diffusible hydrogen content (wt. ppm) | Degree of the degradation in elongation | Method of H-charging | Ref. |
|---|---|---|---|---|
| Fe–22Mn–0.6C | 4.2–12.0 | – | Changing after deformation | [22] |
| Fe–18Mn–0.6C | 1.0–1.7 | 70% → 40–60% | In situ charging | [23] |
| Fe–18Mn–0.6C | 4.3 | 60% → 45% | Pre-charging | [26] |
| Fe–18Mn–1.2C | 1.1 | 80% → 50% | In situ charging | [29] |

properties of a TWIP steel were not strongly affected by hydrogen-precharging even when exposed to extremely severe loading conditions where the hydrogen was introduced by cathodic charging at 100 A $m^{-2}$ in a 1 N $H_2SO_4$ electrolyte with an addition of 10 mg $l^{-1}$ $As_2O_3$ at room temperature, although it showed some hydrogen-assisted surface cracking. From the viewpoint of hydrogen uptake, there are two factors affecting the embrittlement behavior, namely the diffusible hydrogen content and the depth of the hydrogen-affected zone. Even if a significant amount of hydrogen is introduced, hydrogen-assisted cracking cannot propagate to specimen regions reaching deeper than the near-surface hydrogen-affected zone. The hydrogen-affected zone of TWIP steels is determined by the diffusion coefficient and the charging time [24]. Since the diffusion coefficient of hydrogen in an austenitic TWIP steel at room temperature is $1.29 \times 10^{-13}$ $m^2$ $s^{-1}$ and is, hence, much lower than that in conventional ferritic high-strength steels [49], hydrogen charging requires considerable time to obtain a sufficiently large hydrogen-affected zone in the case of static pre-charging. On the one hand, hydrogen charging under ongoing deformation provides a deeper hydrogen-affected zone through the motion of hydrogen-decorated dislocations. Additionally, the diffusible hydrogen content of 5.22 wt. ppm shown in Fig. 3 is significant compared to conventionally reported diffusible hydrogen contents where hydrogen embrittlement of TWIP steels was observed as shown in Table 2 [22–26,29]. The reasons why the diffusible hydrogen content in the present experiment is higher than that observed in our previous study [29] are due to two factors, namely (1) the effect of pre-strain-induced dislocations and deformation twins which are the trapping sites for diffusible hydrogen and (2) the longer total time for hydrogen charging due to the lower strain rate of $1.7 \times 10^{-6}$ $s^{-1}$ (the strain rate used in the previous study was $5.1 \times 10^{-5}$ $s^{-1}$). As a result, the tensile testing conducted under ongoing hydrogen charging resulted in a clear reduction of the maximum attainable elongation.

### 4.2. Contribution of deformation twinning to intergranular fracture

The major sites of hydrogen-assisted cracking are the grain boundaries as shown in Fig. 5a. Hydrogen-assisted intergranular cracking is a generally reported feature of TWIP steels [20,21]. The crack nucleation sites for the intergranular fracture are the grain boundary triple junction and grain boundaries that are intercepted by progressing deformation twins as shown in Fig. 6a and b. The crack initiation at triple junctions is typical in stress corrosion cracking [50] and hydrogen embrittlement [51] of fcc materials. Both high stress concentration and high accumulation of hydrogen at grain-boundary triple junctions are likely reasons for the hydrogen-assisted intergranular cracking at these sites [51]. The stress concentration can be caused by deformation bands that occur at triple junctions [51]. However, even without the effect of plastic deformation bands ending at these defects, the elastic mismatch is also largest at triple junctions. When stress concentrations occur at triple junctions of grain boundaries, diffusible hydrogen moves spontaneously to the vicinity of the stress concentration [51].

The propagation direction of the main crack was perpendicular to the tensile axis as shown in Fig. 4. This indicates that the macroscopic crack propagation direction is determined by the relationship between the tensile axis and the normal of the cracked boundary, since the tensile stress is applied most effectively on the cracked boundary when the normal of the boundary is parallel to the tensile axis. However, in some cases, the intergranular cracking propagates nearly parallel to the tensile axis (Fig. 7) and correlates with the local arrangements of the deformation twins (Fig. 8). These characteristics of intergranular cracking must be correlated with the cracking observed at grain boundaries that intercept the progressing deformation twins as shown in Fig. 6b. An important effect in that context is the stress concentration field at the tip of the expanding deformation twin. The stress concentration can cause intergranular cracking even without hydrogen charging, specifically when the deformation twinning is intercepted at a grain boundary [30,52,53]. The crack initiation at the grain boundary intercepting deformation twins is also considered to be caused by this stress concentration effect. The arrows in Fig. 7 indicate the preferential twinning directions in grains A, B, C and D. The deformation twinning was intercepted at the cracked grain boundaries. The interception of deformation twins assisted the intergranular cracking along the tensile axis. More specifically, the grain boundaries intercepting deformation twins can act as preferential crack initiation sites and as propagation paths. Fig. 11 reveals that cracking did not occur at grain boundaries between grain-pairs with a near-$\langle 100 \rangle$ tensile orientation joint. This observation corresponds to the occurrence of twinning-assisted intergranular cracking, since the initiation of deformation twinning is difficult in $\langle 100 \rangle$ tensile orientations of high-Mn austenitic steels [33,54,55].

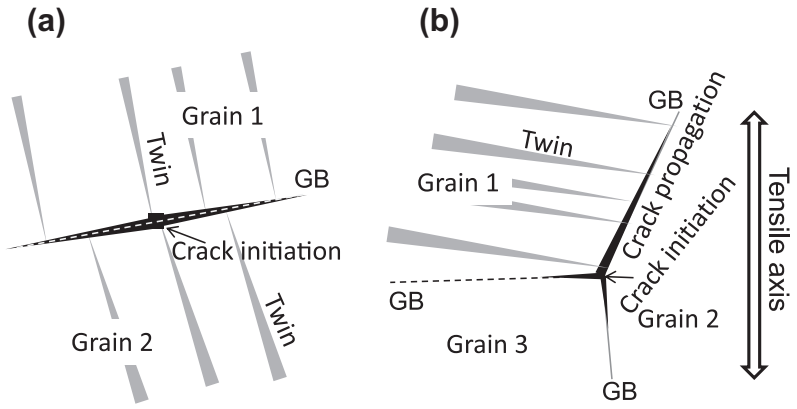


Fig. 12. A schematic describing the relationship between deformation twin and intergranular crack propagation. (a) Cracking is initiated by intercepting deformation twinning. (b) Cracking occurs at the triplets of grain boundaries. In both cases, deformation twins assist the crack propagation.

The crack initiation and propagation phenomena occurring along the grain boundaries are summarized schematically in Fig. 12. As mentioned above, the preferential initiation sites for intergranular cracking are grain boundaries intercepting progressing deformation twins (Fig. 12a) and grain boundary triple junctions. The intergranular crack propagation in both sites is assisted by deformation twinning through the stress concentration at the tip of the deformation twin.

### 4.3. Possible mechanisms of twin boundary cracking

All of the brittle cracks were aligned along non-coherent grain boundaries or twin boundaries except for intersections between cracks and deformation twins. Thus, hydrogen-assisted cracking of TWIP steels can be classified into grain-boundary-assisted and twin-boundary-assisted cracking phenomena. Approximately 25% of all cracks were deformation twin-boundary-assisted cracking events. This fact indicates that although intergranular cracking is the dominant effect, deformation twin boundary cracking is essential for the hydrogen embrittlement mechanism of TWIP steels. In this section, we hence discuss the mechanism of twin boundary cracking in more detail.

Fig. 11 shows that twin boundary cracking occurred only among grain pairs with tensile orientations near-$\langle 1\,1\,1\rangle$ or $\langle 1\,1\,0\rangle$. Since the deformation twin boundary cracking path was oriented dominantly along the primary and secondary deformation twin boundaries as shown in Fig. 9, the crystallographic orientation dependence of the observed cracking behavior is correlated with the deformation twinning behavior. More specifically, deformation twinning occurs preferably when the tensile orientation is close to $\langle 1\,1\,1\rangle$ or $\langle 1\,1\,0\rangle$ [33,54,55].

The deformation twin boundaries can act as crack initiation sites as well as propagation paths as shown in Fig. 10. Deformation twin boundary cracking has even been reported in steels that were not exposed to any artificial hydrogen charging [31,56,57]. Twin boundary cracking requires a sufficient stress concentration to initiate failure at the obstacle deformation twin boundary that is associated with the twin–twin interaction [31]. The possible interactions are (1) the interception of deformation twinning at an already existing obstacle deformation twin boundary, and (2) the intersection of two simultaneously active deformation twins proceeding on different twinning planes. According to the Olson–Cohen mechanism [58], α'-martensite has been reported to form at such an intersection of deformation twins in metastable austenitic steels [59,60]. These small portions of α′-martensite can act as hydrogen-assisted crack initiation sites [61]. However, the austenite phase of the present steel is stabilized by the addition of a very high concentration of carbon, and hence, the formation of α′-martensite is not plausible in this case. Therefore, in the present study, the interception of deformation twinning at an existing twin boundary that acts as an obstacle appears to be a more reasonable explanation than the intersection mechanism for crack initiation. More specifically, the stress concentration at the tip of a blocked deformation twin, when running into the obstacle deformation twin boundary, is very high. Such a high stress peak is required to intersect the obstacle twin boundary [62,63]. To quantify this situation we assume that proceeding deformation twins can be approximated as a moving disclination dipole [31,57,64]. Then, the tensile stress field around the tip of the deformation twins acting on an obstacle twin boundary can be estimated by the following equation [31]:

$$\sigma_{xx}|_{x=0} = D\omega \ln \frac{|y-a|}{|y+a|} \tag{1}$$

where $D = G/2\pi(1-\nu)$, $G$ is the shear modulus, $\nu$ is the Poisson's ratio, $\omega$ is the power of the disclinations, and $2a$ is the twin thickness. The geometrical relationship expressed in Eq. (1) is described in Fig. 13. The stress becomes extremely high for a spacing of $y \approx -a$, causing cracking on the affected obstacle twin boundary. When cracking occurs, an additional stress at the crack tip promotes the propagation of the twin boundary cracking [31].

The deformation twin boundary cracking processes are schematically described in Fig. 14. The hydrogen-assisted

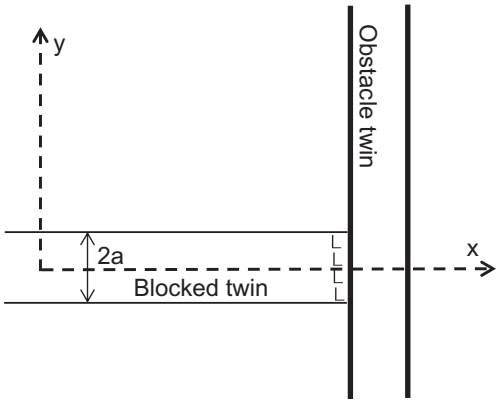


Fig. 13. Schematic describing the parameters in Eq. (1).

cracking starts at the deformation twin boundary (Fig. 14a) or at a non-coherent grain boundary (Fig. 14b). Even if cracking is initiated at a grain boundary, e.g. at a grain boundary triple junction, the propagation path can change from the non-coherent grain boundary to a deformation twin boundary alignment. This type of transition was indeed observed in Fig. 8. Thus, deformation twin boundaries can provide an important crack propagation path even when the crack was originally initiated on a non-coincident grain boundary.

We have to note here a certain contradiction of this observation with respect to the common notion, namely that coherent Σ3 twin boundaries are known to act as a common crack arrest site for delayed fracture in Fe–Cr–Ni austenitic steel. This is commonly attributed to the fact that coherent Σ3 twin boundaries are highly ordered and hence energetically stable [65,66]. Additionally, coherent boundaries such as the fcc Σ3 twin boundary are not preferred hydrogen-trapping sites, implying that hydrogen does not preferentially weaken the twin boundary strength as compared to non-order grain boundaries which can be highly affected and weakened. However, hydrogen was reported to be trapped at the deformation twin boundaries of Fe–Mn–C TWIP steels [67,68], and both annealing twin boundary cracking and deformation twin boundary cracking were observed as shown in Figs. 9 and 10. In order to resolve this apparent contradiction we discuss the four factors that promote hydrogen-assisted deformation twin boundary cracking in Fe–Mn–C TWIP steels.

First, very high stress concentration peaks exist at the tip of moving deformation twins when interfering with an obstacle deformation twin boundary as discussed in terms of Eq. (1) and as schematically shown in Fig. 15a. When coherent boundaries act as hydrogen-trapping sites, a local strain field is required to trap hydrogen there. The stress concentration at the tip of a moving deformation twin provides this local strain field, which attracts hydrogen to the obstacle deformation twin boundary. Therefore, the stress concentration field at the twin tip is essential for the localization of hydrogen as well as crack initiation on grain and twin boundaries.

The second factor is the dislocation–twin interaction. Mahajan et al. [69] and Remy et al. [70] reported that dislocations intersect twin boundaries through a dislocation dissociation mechanism. An example of the dislocation reaction is as follows [69]:

$$1/2[\bar{1}\,0\,1](1\,1\,1) \rightarrow 1/6[\bar{1}\,1\,4](\bar{5}\,\bar{1}\,\bar{1}) + 1/6[\bar{2}\,\bar{1}\,\bar{1}](\bar{1}\,1\,1) \qquad (2)$$

where the $(\bar{1}\,1\,1)$ plane is the obstacle twin boundary. The formation of $1/6[\bar{2}\,\bar{1}\,\bar{1}]$ dislocations creates slip steps on the obstacle twin boundary [71], disturbing the coherency of the twin boundary. As a result, a strain field is formed at these deformation steps, promoting hydrogen trapping on the twin boundaries as shown in Fig. 15b. In carbon-containing TWIP steels, the dislocation multiplication rate is much greater than in carbon-free alloys, probably due to the carbon–manganese dipole [72]. This effect suggests that the frequency of dislocation–twin interactions is significantly greater in carbon-containing TWIP steels than in carbon-free fcc alloys.

The third factor is associated with the position of interstitial carbon atoms. The carbon position is on the

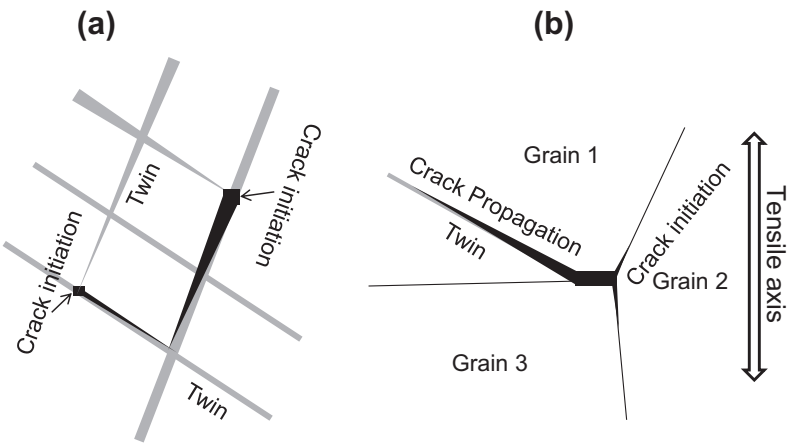


Fig. 14. Schematics expressing twin boundary cracking and its propagation. (a) Cracking associated with twin–twin interactions. (b) Change in crack propagation path from the grain boundary to the deformation twin boundary.

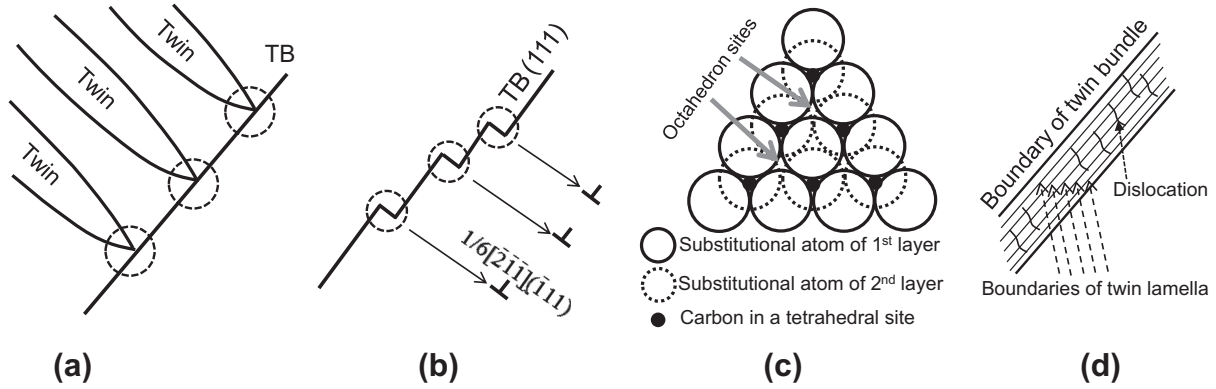


Fig. 15. Schematics describing the factors affecting hydrogen trapping at the deformation twin boundaries. TB: Twin boundary. (a) Stress concentration at a tip of a deformation twin. (b) Strain field at the steps formed by the dislocation–twin intersection. (c) Lattice distortion due to pseudo-twin formation. In (c), the interstitial carbons exist at the tetrahedral sites in a twin, and the grey arrows indicate octahedral sites that are the carbon positions in the parent crystals. (d) Nanoscale structure of deformation twins that includes dislocations and nanotwin plates.

octahedral interstitial site in austenitic steels. Adler et al. suggested [73] that this position of carbon may change from an octahedral to a tetrahedral site when a leading partial dislocation passes through a position where interstitial carbon is located. Since deformation twinning propagates by the motion of leading partials, the structure of the deformation twin boundary of carbon-containing fcc alloys is affected by the change in the carbon position. The carbon position in a carbon-containing deformation twin is schematically shown in Fig. 15c. The change in the carbon position from an octahedral to a tetrahedral site leads to lattice distortions in the deformation twin. In contrast, the untwinned matrix does not experience any significant lattice distortion, since the carbon remains on the octahedral site. A deformation twin involving the deviating carbon positions is referred to as a pseudo-twin owing to the loss of its full mirror symmetry [73]. The lattice mismatch arising from the difference in the lattice distortion produces a local elastic strain on the pseudo-twin boundary. The appearance of such an elastic strain may promote hydrogen trapping on the deformation twin boundaries. However, this factor only applies to carbon-containing alloys with low stacking fault energy, such as the TWIP steel studied here.

The fourth reason is the considerable number of lattice defects that exits in and around deformation twins [25,31,32,74–79]. Deformation twins in Fe–Mn–C austenitic steels actually form twin bundles, which are composed of numerous dislocations and nanotwins [25,80] as schematically shown in Fig. 15d, rather than isolated twins. Such a feature was also observed in Fig. 5d. Dislocations are prominent reversible hydrogen trapping sites [25,65], and nanotwin boundaries can also act as hydrogen trapping sites due to the three above-mentioned factors. Thus, it is plausible that diffusible hydrogen can indeed localize at deformation twins. The first and second factors apply both to deformation twin boundaries and also to annealing twin boundaries while the third and fourth factors apply specifically to deformation twins.

### 4.4. Further hydrogen effects on embrittlement

The contribution of deformation twins to the hydrogen embrittlement was discussed in the previous section. However, we cannot rule out further interactions of hydrogen with other lattice defects such as vacancies [12] and dislocations [13–16] as well as its effects on the cohesive energy of grain boundaries [9–11]. Since these interactions essentially cause hydrogen embrittlement of steels even without the presence of deformation twins, deformation twinning is considered to essentially assist these other possible embrittlement effects that are associated with one or more of these interactions. In particular, hydrogen–dislocation interactions affecting dislocation motion [13–16,81–86] and twinning behavior [87,88] have been reported to be relevant in fcc alloys including specifically austenitic steels. In this section, we, therefore, introduce some facts that could be related to the present results.

First, we note that previous investigations that used the same experimental set-up as this work have revealed that hydrogen charging did not affect the work-hardening behavior of TWIP steels, even though clear hydrogen embrittlement was detected [21,23,29]. This is an essential point since it reveals that if the hydrogen–dislocation interaction would be the dominant embrittlement reason in the current case of austenitic TWIP steels, the stress–strain response, specifically the strain-hardening characteristics should have been changed accordingly [81–83]. Moreover, the work-hardening rate changes most profoundly when the twinning behavior changes [27,34,36,89,90]. Therefore, an observation of no significant change in the work-hardening behavior indicates that hydrogen–dislocation interactions are not the major cause of the hydrogen embrittlement in the present case. Instead, the occurrence of embrittlement is considered here to require a reduction in the cohesive energy of each boundary arising from hydrogen, since the reduction in cohesive energy can lead to hydrogen-assisted cracking without any changes in the stress–strain responses of the material.

However, we also have to note that the dominant trap site of diffusible hydrogen in TWIP steels are the dislocations [25,65], and the diffusible hydrogen content is the controlling factor of hydrogen embrittlement [23,25]. These facts indicate that hydrogen–dislocation interactions will also to some extent assist the embrittlement in the current case. In terms of hydrogen–dislocation interactions, some phenomena affecting dislocation motion have been reported in the literature: (i) a decrease in the activation barriers of dislocation motion [83]; (ii) enhancement of dislocation planarity arising from stabilization of the edge components [84]; (iii) a reduction in the staking fault energy [91,92]; (iv) the reduction in the elastic interactions among the dislocations [85]; and (v) the reduction in shear modulus [86].

All these phenomena were examined in fcc materials such as pure Ni and austenitic stainless steels. Hence, the enhanced dislocation mobility may cause strain localization on non-coherent grain boundaries and coherent Σ3 twin boundaries in TWIP steels, which can assist hydrogen embrittlement.

### *4.5. Al effect on hydrogen embrittlement in terms of deformation twinning*

Al addition has been reported to improve the hydrogen embrittlement properties of Fe–Mn–C high-strength TWIP steels [18,25,26,39,68]. The hydrogen embrittlement properties of such Al-containing TWIP steels were examined in terms of delayed fracture tests that were conducted on cup-drawn specimens [18]; tensile tests conducted after hydrogen precharging [25,26]; and tensile tests under ongoing hydrogen charging [39,68]. All the results obtained from these experiments revealed that Al plays a key role in preventing hydrogen embrittlement. Two important possible reasons were suggested for the effect of Al on the hydrogen embrittlement. First, the Al addition provides an $Al_2O_3$ layer on the sample surface, preventing hydrogen entry [26]. The reduction in the total hydrogen uptake consequently suppresses hydrogen embrittlement. A second line of thought is that the Al addition suppresses deformation twinning due to the decrease in the stacking fault energy, preventing twin boundary cracking [68]. The present work supports the second line of argumentation, i.e. the effect of Al on deformation twinning, since the contribution of deformation twins on hydrogen-assisted cracking was indeed revealed in our current experiments. Additionally, the Al addition is considered to suppress intergranular cracking as well as the twin boundary cracking in terms of twinning-assisted intergranular cracking as also observed in the present work.

## 5. Conclusions

We observed hydrogen-assisted cracking and crack propagation in a Fe–18Mn–1.2C TWIP steel using a slow-strain-rate tensile test under ongoing hydrogen charging and ECCI. We show that deformation twinning plays an important role in the hydrogen embrittlement of TWIP steels. The main conclusions are:

(1) Hydrogen embrittlement occurred during tensile testing under ongoing hydrogen charging, producing clear intergranular and transgranular cracking with a considerable amount of associated subcracks. The hydrogen-assisted intergranular cracking was even observed on Σ3 coherent annealing twin boundaries. The crack initiation sites were deformation twin boundaries as well as non-coherent grain boundaries. The cracks were observed to propagate along both non-coherent grain boundaries and deformation twin boundaries depending on the deformation twin morphology relative to the loading axis.
(2) Preferred crack nucleation sites for intergranular cracking were a grain boundary triple junction and a grain boundary impinging on a deformation twin. In cases when the deformation twin density was low or the major twinning direction was nearly parallel to the grain boundary, either the intergranular cracking stopped or the propagation path changed from a non-coherent grain boundary to a deformation twin boundary. Even when intergranular cracking occurred, deformation twinning played an important role in assisting its propagation owing to the very high stress concentration at the twin tip.
(3) In contrast, deformation twin boundary cracking was caused by twin–twin interaction, e.g. by the interception of deformation twinning at an already existing deformation twin. Deformation twin boundary cracking propagated along both primary and secondary deformation twin boundaries with a zigzag-type path. Deformation twin boundary cracking was observed particularly along grain boundaries pertaining to grain pairs with near-⟨1 1 1⟩ and ⟨1 1 0⟩ tensile orientations, since ⟨1 1 1⟩ and ⟨1 1 0⟩ are preferential tensile orientations for deformation twinning in austenitic steels.

## Acknowledgements

The authors gratefully acknowledge the financial support by the Elements Strategy Initiative for Structural Materials (ESISM) through the Ministry of Education, Culture, Sports, Science and Technology (MEXT) of Japan. M.K. acknowledges the Research Fellowship of the Japan Society for the Promotion of Science for Young Scientists. The Materials Manufacturing and Engineering Station and Materials Analysis Station at the National Institute for Materials Science supported this work through the production of the samples and the analysis of the chemical compositions.

## References


[1] Louthan Jr MR, Caskey Jr GR, Donovan JA, Rawl Jr DE. Mater Sci Eng 1972;10:357.
[2] Daw MS, Baskes MI. Phys Rev Lett 1983;50:1285.
[3] Akiyama E. ISIJ Int 2012;52:307.
[4] Toribio J, Elices M. Int J Solids Struct 1991;28:791.
[5] Takagi S, Toji Y, Yoshino M, Hasegawa K. ISIJ Int 2012;52:316.
[6] Luppo MI, Garcia JO. Corros Sci 1991;32:1125.
[7] Carneiro RA, Ratnapuli RC, Lins Vde FC. Mater Sci Eng A 2003;357:104.
[8] Wang M, Akiyama E, Tsuzaki K. Scripta Mater 2005;52:403.
[9] Troiano AR. Trans ASM 1960;52:54.
[10] Oriani RA. Ann Rev Mater Sci 1978;8:327.
[11] Hirth JP. Metal Trans A 1980;11A:861.
[12] Nagumo M, Yagi T, Saitoh H. Acta Mater 2000;48:943.
[13] Birnbaum HK, Sofronis P. Mater Sci Eng A 1994;176:191.
[14] Robertson IM, Birnbaum HK. Acta Metall 1986;34:353.
[15] von Pezold J, Lymperakis L, Neugebauer J. Acta Mater 2011;59:2969.
[16] Maxelon JM, Pundt A, Pyckhout-Hintzen W, Barker J, Kirchheim R. Acta Mater 2001;59:2625.
[17] Scott C, Allain S, Faral M, Guelton N. Rev Metal Cah D Inf Tech 2006;103:293.
[18] De Cooman BC, Chin K-G, Kim J. In: Chiaberge Marcello, editor. High Mn TWIP steels for automotive applications, new trends and developments in automotive system engineering. InTech; 2011. ISBN 978-953-307-517-4.
[19] Ćwiek J. J AMME 2009;37:193.
[20] Chin K-G, Kang C-Y, Shin S-Y, Hong S, Lee S, Kim HS, et al. Mater Sci Eng A 2011;528:2922.
[21] Koyama M, Akiyama E, Tsuzaki K. Corros Sci 2012;54:1.
[22] Koyama M, Akiyama E, Tsuzaki K. Scripta Mater 2012;66:947.
[23] Koyama M, Akiyama E, Tsuzaki K. Corros Sci 2012;59:277.
[24] Ronevich JA, Kim SK, Speer JG, Matlock DK. Scripta Mater 2012;66:956.
[25] Chun YS, Park K-T, Lee CS. Scripta Mater 2012;66:960.
[26] Park I-J, Jeong K-H, Jung J-G, Lee CS, Lee Y-K. Int J Hydrogen Energy 2012;37:9925.
[27] Steinmetz DR, Jäpel T, Wietbrock B, Eisenlohr P, Gutierrez-Urrutia I, Saeed-Akbari A, et al. Acta Mater 2013;61:494.
[28] Chun YS, Kim JS, Park K-T, Lee Y-K, Lee CS. Mater Sci Eng A 2012;533:87.
[29] Koyama M, Akiyama E, Sawaguchi T, Raabe D, Tsuzaki K. Scripta Mater 2012;66:459.
[30] Doepken HC. Trans AIME 1952;194:166.
[31] Müllner P, Solenthaler C, Uggowitzer PJ, Speidel MO. Acta Metall Mater 1994;42:2211.
[32] Gutierrez-Urrutia I, Zaefferer S, Raabe D. Scripta Mater 2009;61:737.
[33] Gutierrez-Urrutia I, Zaefferer S, Raabe D. Mater Sci Eng A 2010;527:3552.
[34] Gutierrez-Urrutia I, Raabe D. Acta Mater 2011;59:6449.
[35] Sasaki T, Watanabe K, Nohara K, Ono Y, Kondo N, Sato S. Trans Iron Steel Inst Jpn 1982;22:1010.
[36] Koyama M, Sawaguchi T, Tsuzaki K. ISIJ Int 2013;53:323.
[37] Frankel GS, Latanision RM. Metal Trans A 1986;17A:869.
[38] Tien JK, Thompson AW, Bernstein IM, Richards RJ. Metal Trans A 1976;7A:821.
[39] Koyama M, Akiyama E, Tsuzaki K. ISIJ Int 2012;52:2283.
[40] Takai K, Watanuki R. ISIJ Int 2003;43:520.
[41] Dastur YN, Leslie WC. Metal Trans A 1981;12A:749.
[42] Chen L, Kim H-S, Kim S-K, De Cooman BC. ISIJ Int 2007;47:1804.
[43] Lee S-J, Kim J, Kane SN, De Cooman BC. Acta Mater 2011;59:6809.
[44] Koyama M, Sawaguchi T, Tsuzaki K. Mater Trans 2012;53:546.
[45] Koyama M, Sawaguchi T, Tsuzaki K. Philos Mag 2012;92:3051.
[46] Seol J-B, Jung JE, Jang JW, Park CG. Acta Mater 2013;61:558.
[47] Remy L. Acta Metall 1978;26:443.
[48] Koyama M, Sawaguchi T, Ogawa K, Kikuchi T, Murakami M. Mater Trans 2010;51:1194.
[49] Kim SK, Oh PY, Jeon S-H, Han SH, Kang SE, Chin K-G, et al. Gent, Steely hydrogen conference proceedings; 2011. p. 189.
[50] Cheung C, Erb U, Palumbo G. Mater Sci Eng A 1994;185:39.
[51] Wilcox BA, Smith GC. Acta Metall 1965;13:331.
[52] Lemy L. Metall Trans A 1981;12A:387.
[53] Tomota Y. Tetsu-to-hagane 1991;77:315.
[54] Karaman I, Sehitoglu H, Gall K, Chumlyakov YI, Maier HJ. Acta Mater 2000;48:1345.
[55] Ueji R, Tsuchida N, Terada D, Tsuji N, Tanaka Y, Takemura A, et al. Scripta Mater 2008;59:963.
[56] Abraham DP, Altstetter CJ. Metal Mater Trans A 1995;26A:2859.
[57] Müllner P. Mater Sci Eng A 1997;234–236:94.
[58] Olson GB, Cohen M. Metall Trans A 1975;6:791.
[59] Inamura T, Takashima K, Higo Y. Philos Mag 2003;83:935.
[60] Nakada N, Ito H, Matsuoka Y, Tsuchiyama T, Takaki S. Acta Mater 2010;58:895.
[61] Zhang L, Wen M, Imade M, Fukuyama S, Yokogawa K. Acta Mater 2008;56:3414.
[62] Mahajan S, Barry DE, Eyre BL. Philos Mag 1970;21:43.
[63] Remy L, Pineau A. Mater Sci Eng 1977;28:99.
[64] Armstrong RW. Science 1968;162:799.
[65] Gertsman VY, Bruemmer SM. Acta Mater 2001;49:1589.
[66] Watanabe T, Tsurekawa S. Acta Mater 1999;47:4171.
[67] So KH, Kim JS, Chun YS, Park K-T, Lee Y-K, Lee CS. ISIJ Int 2009;49:1952.
[68] Ryu JH, Kim SK, Lee CS, Suh D-W, Bhadeshia HKDH. Proc Roy Soc A 2013;469. http://dx.doi.org/10.1098/rspa.2012.0458.
[69] Mahajan S, Chin GY. Acta Metall 1973;21:173.
[70] Remy L. Acta Metal 1977;25:711.
[71] Wang YB, Sui ML. Appl Phys Lett 2009;94:021909.
[72] Hutchinson B, Ridley N. Scripta Mater 2006;55:299.
[73] Adler PH, Olson GB, Owen WS. Metal Trans A 1986;17A:1725.
[74] Eisenlohr A, Gutierrez-Urrutia I, Raabe D. Acta Mater 2012;60:3994.
[75] Allain S, Chateau JP, Bouaziz O. Mater Sci Eng A 2004;387–389:143.
[76] Bouaziz O, Allain S, Scott C. Scripta Mater 2008;58:484.
[77] Barbier D, Gey N, Allain S, Bozzolo N, Humbert M. Mater Sci Eng A 2009;500:196.
[78] Sevillano JG. Scripta Mater 2009;60:336.
[79] Gutierrez-Urrutia I, Raabe D. Acta Mater 2012;60:5791.
[80] Idrissi H, Renard K, Ryelandt L, Schryvers D, Jacques PJ. Acta Mater 2010;58:2464.
[81] Abraham DP, Altstetter CJ. Metall Mater Trans A 1995;26A:2859.
[82] Ulmer DG, Altstetter CL. Acta Metall Mater 1991;39:1237.
[83] Birnbau HK. Scripta Metall Mater 1994;31:149.
[84] Ferreira PJ, Robertson IM, Birnbaum HK. Acta Mater 1999;47:2991.
[85] Ferreira PJ, Robertson IM, Birnbaum HK. Acta Mater 1998;46:1749.
[86] Nibur KA, Bahr DF, Somerday BP. Acta Mater 2006;54:2677.
[87] Astafurova EG, Zakharova GG, Maier HJ. Scripta Mater 2010;63:1189.
[88] Kireeva IV, Chumlyakov YI, Tverskov AV, Maier H. Tech Phys Lett 2011;37:522.
[89] Koyama M, Murakami M, Ogawa K, Kikuchi T, Sawaguchi T. Mater Trans 2007;48:2729.
[90] Koyama M, Sawaguchi T, Lee T, Lee CS, Tsuzaki K. Mater Sci Eng A 2011;528:7310.
[91] Ferreira PJ, Robertson IM, Birnbaum HK. Mater Sci Forum 1996;207:93.
[92] Pontini AE, Hermida JD. Scripta Mater 1997;37:1831.